JMEPEG (2023) 32:1333–1346
https://doi.org/10.1007/s11665-022-07160-1

1059-9495/$19.00

TECHNICAL ARTICLE

The Forming Control Method of Ni35A + TiC Composite Coatings on Cylindrical Substrate Deposited by Laser Cladding

Zhaozhen Liu, Guofu Lian, Chenmin Zhao, Jinmin Peng, and Yang Zhang

Submitted: 20 August 2021 / Revised: 16 May 2022 / Accepted: 28 May 2022 / Published online: 3 August 2022

This paper explored the influence of process parameters of laser cladding Ni35A + TiC composite coatings on the width, height, cross-sectional area, and wetting angle of single-track cladding on the cylindrical substrate by establishing prediction models based on Response Surface Methodology. The clad width was increased initially then flattened; however, increasing scanning speed and gas flow decreased the clad width. Accelerating scanning speed caused a reduction of clad height; increasing gas flow resulted in the increase of clad height. The cross-sectional area was broadened by larger laser power and gas flow, but the cross-sectional area was reduced under a faster scanning speed. A wider wetting angle was created by accelerating scanning speed and reducing gas flow. The process parameters were optimized and experimentally validated. The error rates for the width, height, cross-sectional area, and wetting angle were 3.702, 2.451, 6.094, and 0.085% respectively, indicating remarkable prediction accuracy.

Keywords composite coatings, forming control, laser cladding, Ni35A + TiC

1. Introduction

Laser cladding is also known as Direct Metal Deposition (DMD), Laser Metal Deposition (LMD), or Direct Energy Deposition (DED) (Ref 1). The principal process is to use the high-density energy generated by laser irradiating the substrate to create a molten pool (Ref 2, 3). Simultaneously, the cladding material is injected into the molten pool. With the movement of the laser beam, the cladding material is melted and solidified rapidly. A metallurgical bond with the substrate is formed and the coatings with improved surface properties in terms of wear and corrosion resistance are created. Laser cladding is featured by its low heat-affected zones, high forming accuracy, and exceptional metallurgical bonding compared to other surface coating technologies such as electrodeposition, physical/chemical vapor deposition, and thermal spraying. Thus, the technology has been widely applied in surface enhancement, restoration, and remanufacturing (Ref 4-8). As a complex process, the process parameters in laser cladding, such as laser power, scanning speed, and powder feeding rate have significant impact on the morphology of the cladding layer (Ref 9). The following studies explored the coupling effects between process parameters and the cladding morphology on the planar and cylindrical substrates.

There are numerous studies on the planar substrate. Shayanfar et al. deposited Inconel 625 on ASTMA592 steel substrate by using laser cladding process. To optimize and predict the quality of the obtained coating, the empirical-statistical method was employed to analyze the relationships between the coating geometries for each sample (width, height, wetting angle, and dilution) and cladding parameters (laser power, scanning rate, and powder feeding rate). These relationships were used to extract a process map to obtain the optimal process parameters (Ref 10). Javid et al. investigated the laser cladding process of WC on Inconel 718 by preplacing the powder. Response surface methodology was adopted to explore the influence of process parameters on the properties of cladding layers and achieved a cladded layer of proper geometry with minimum dilution, porosity, and highly efficient process. A validation experiment was carried out to verify the influence of laser power on the clad width and porosity (Ref 11). Fan et al. aimed at optimizing the process of tungsten carbide (WC)-reinforced Co50 ceramic composite coating by laser cladding. They used a single-factor experiment to probe the variation of the geometrical size, dilution rate, and hardness of cladding layers by altering the process parameters. An orthogonal experiment was designed to explore the optimal parameters for the laser cladding process by taking the hardness and dilution rate of the coatings as comprehensive indexes. Based on the results of the experiment, the mathematical model of the relationship between the process parameters and the geometrical size of the cladding layers was constructed by regression analysis (Ref 12). Khorram et al. prepared Inconel 718 superalloy by laser cladding. Response Surface Methodology was applied to investigate the relationship between process parameters and responses, where the laser frequency, pulse width, and scanning speed served as the input variables and the geometry of the deposited beads (width, height, and

Zhaozhen Liu, Guofu Lian, Chenmin Zhao, and **Jinmin Peng**, School of Mechanical and Automotive Engineering, Fujian University of Technology, Fuzhou 350118, China; and **Yang Zhang**, School of Engineering + Technology, Western Carolina University, Cullowhee, NC 28723. Contact e-mail: gflian@mail.ustc.edu.cn.

clad angle), dilution ratio, and hardness served as the output responses. The results indicated that the laser frequency and pulse width had a positive effect on the bead width, clad angle, and dilution ratio. The laser frequency and pulse width had a negative effect on the bead height and hardness (Ref 13).

Recently, more scholars have focused on the cylindrical substrate. Bourahima et al. aimed to produce well-bonded Ni-based cladding layers with a very small dilution zone on a non-planar surface (curved section). Multi-track overlapped coatings were prepared on cupro-nickel-aluminum (Cu–Ni–Al) substrate by laser cladding. The ANOVA (Analysis of variance) method was used to investigate the impact of the process parameters such as laser power, scanning speed, and powder feeding rate on the coating geometry. The optimal parameter combination was obtained by the ANOVA analysis to optimize the bonding quality between the Ni coating and the Cu–Ni–Al substrate (Ref 14). Barr et al. adopted an orthogonal experiment design to prepare clad samples under varied laser power, scanning speed, and powder feeding rate. They analyzed the microstructure variation and crack generation mechanism of the cladding layer section. The results demonstrated that cracks in the cladding layer were reduced by decreasing the scanning speed or avoiding excessive laser power (Ref 15). Calleja et al. carried out laser cladding path design and process parameters optimization on the semi-spherical surface. By selecting cladding efficiency, wetting angle, height, and width as indexes, the optimal parameters of the five-axis laser cladding process were achieved by data analysis. A validation experiment was conducted to obtain the cladding layer with good morphology and performance (Ref 16).

Above all, current studies mainly focus on exploring the relationship between geometric characteristics and process parameters of cladding layers on the planar substrate rather than on a composite curved substrate. The curved substrate is different from the plane shape in the morphology, the focusing of powder flow, and the forming mechanism of molten pool. Limited studies were conducted on curved substrates focusing on restoration of shaft parts and restoration path design of arbitrary irregular curved surfaces. These studies provide a theoretical basis for the restoration of curved surfaces. However, there is still a lack of practical guidance due to insufficient cladding experiments on curved surfaces with composite material. Therefore, this research examines the trajectory morphology of composite cladding on curved substrates and establishes the mathematical models between the process parameters and morphology of cladding layers. This study provides practical support for laser cladding technology in curved substrates.

2. Experimental Design

The rotary die-cutting roller was considered as the object of this research. A 45 # cylindrical steel was used as the substrate, with 120 mm diameter and 120 mm length. Ni35A and TiC were selected as the cladding powder, with the particle size ranging from 48 to 106 μm. Table 1 provides the chemical composition of the substrate and the powders. T.C refers to the total carbon and F.C refers to the free carbon. Figure 1 provides the microstructure of the two kinds of powders.

As illustrated in Fig. 2 and 3, the laser cladding equipment includes YLS-3000 laser from IPG of German, FDH037 laser cladding head with 300 mm focal length from lasermech of USA, TFLW-4000WDR-01–3385 water cooler from Tongfei of China, GZ-DPSF-2 pneumatic powder feeding system of Songxing of China, PLC control system from Mitsubishi of Japan, M-710iC/50 industrial robots from FANUC of Japan, and SX14-012PULSE laser pulse waveform control system. Argon was used as the protective gas in the cladding process.

Response Surface Methodology (RSM) is a typical scientific experimental design to establish statistical models (Ref 17). Its principle is to construct a mathematical model with explicit expression to approximate the implicit limit state function through a series of deterministic experiments and reveal the coupling effects between input parameters and output responses. This paper employed the central composite design (CCD) of RSM, which provides the highest accuracy prediction and overall error with minimizing the number of experiments. Laser power (LP), scanning speed (SS), and gas flow (GF) were selected as the input variables and clad width, height, cross-sectional area, and wetting angle were chosen as the output variables. A three-factor five-level matrix was established and presented in Table 2. In this matrix, the five levels of each input factor were coded as ' $-\alpha$, -1, 0, $+1$, $+\alpha$' (α is 2 in this paper) (Ref 18-20).

The substrate was wiped with absolute ethanol before the experiment. Ni35A and TiC powders were mixed in the mass ratio of 1:1 using YXQM-2L planetary mill for 30 min. The mixed powder was dried in a vacuum dryer for 30 min. The cladding process was carried out according to the experimental design. The specimens after cladding were processed by cutting, inlaying, grinding, polishing, and corrosion. The powder feeding speed is controlled by the gas flow with a 30 V constant powder feeding voltage.

The geometric structure of the cladding layer is illustrated in Fig. 4, in which CZ, MZ, HAZ, and SZ indicate the cladding zone, the melting zone, the heat-affected zone, and the substrate, respectively. The geometric characteristics of the cladding layer include the cladding width (W), height (H), and wetting angles on both sides (θ_L and θ_R). Equation (1) shows the calculation of wetting angle θ (Ref 21). Table 3 provides the experimental results including the cladding width, height, cross-sectional area, and wetting angle.

$$\text{Wetting Angle}: \theta = \frac{\theta_L + \theta_R}{2} \quad \text{(Eq 1)}$$

3. Results and Analysis

3.1 Significance Test and Analysis of Variance

This paper explored the forming control method of single-track cladding layers on the cylindrical substrate by studying the width, height, cross-sectional area, and wetting angle. Tables 4, 5, 6, and 7 provide the ANOVA for the cladding width, height, cross-sectional area, and wetting angle. ANOVA analysis is an efficient statistical technique, which allows verifying the impact of the input variables on the responses and the accuracy of the established mathematical models (Ref 22).

Based on Table 4, the P-value in the model suggested for the cladding width was less than 0.0001%, and the lack of fit P-value was greater than 0.05, which indicated that the model had a 0.01% probability at most distorted due to the interference

Table 1 Chemical composition (wt.%) of cladding material

Material	C	Si	O	Fe	Cr	B	T.C	F.C	N	Ni	Mn	Cu
Substrate	0.42–0.50	0.17–0.37	…	Bal	≤ 0.25	-	…	…	…	≤ 0.30	0.50–0.80	≤ 0.25
Ni35A	0.32	3.35	< 0.05	2.75	7.75	1.65	…	…	…	Bal	…	…
TiC	…	0.02	0.50	0.08	…	…	> 18.8	< 0.50	0.50	…	…	…

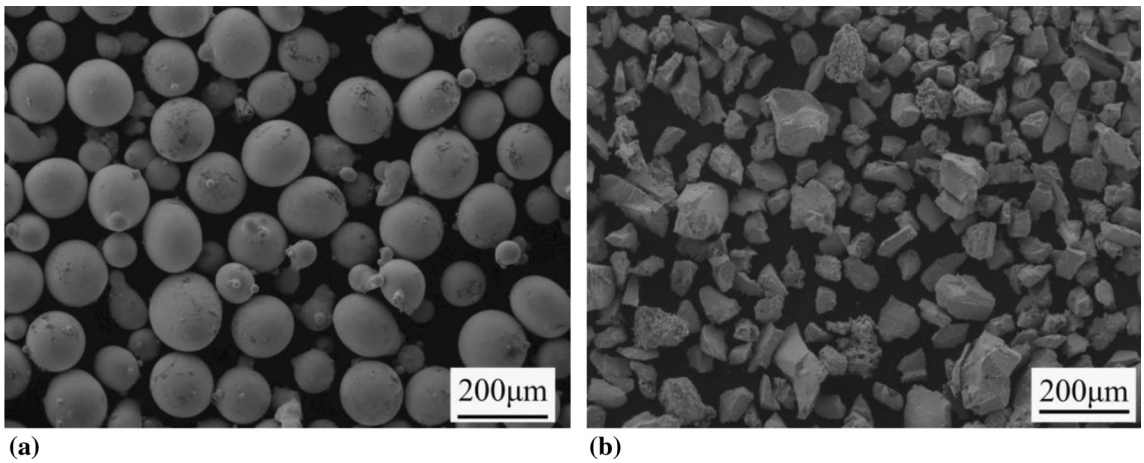

Fig. 1 (a) Microstructure of Ni35A; (b) Microstructure of TiC

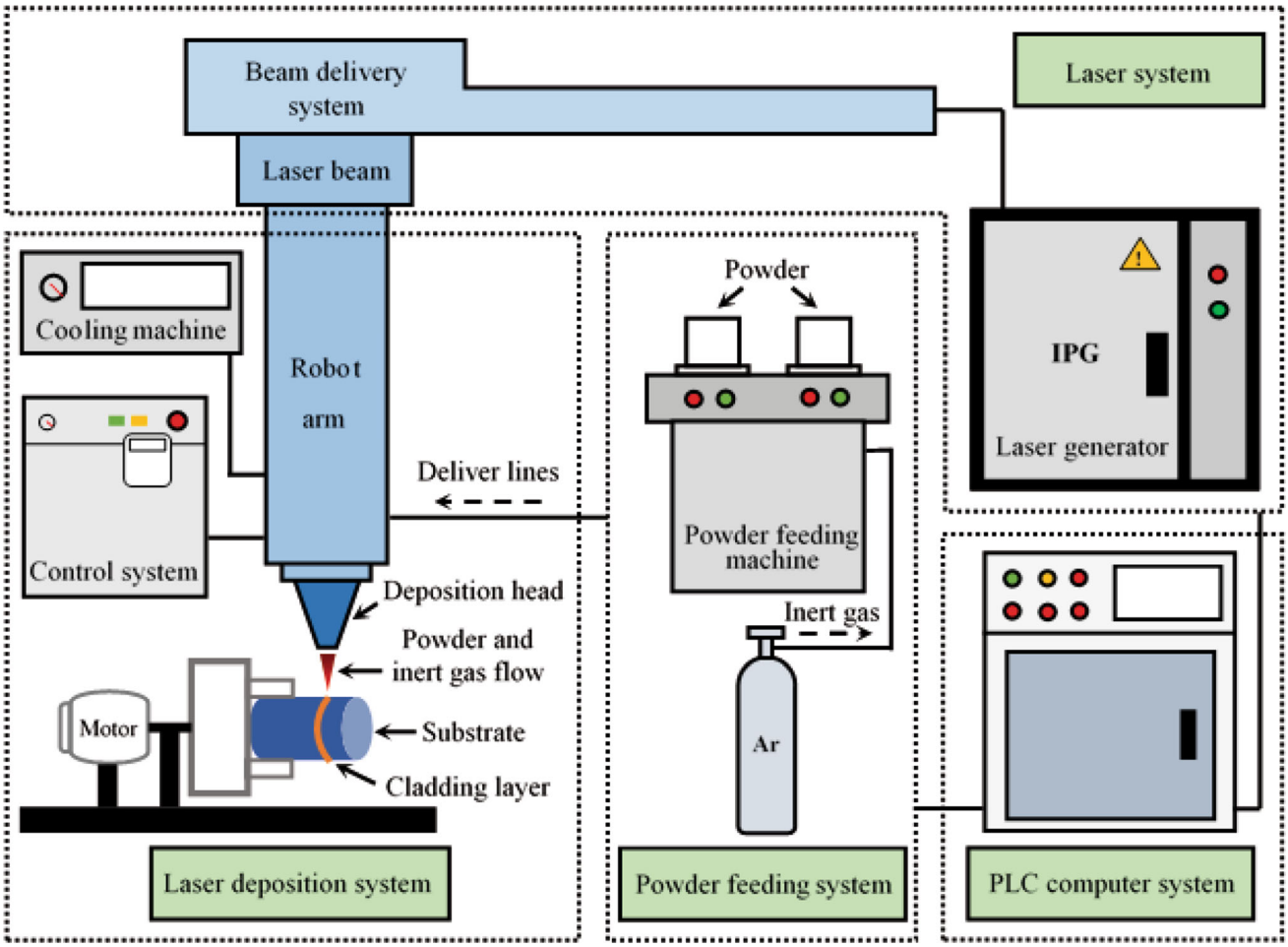

Fig. 2 Schematic illustration of laser cladding equipment

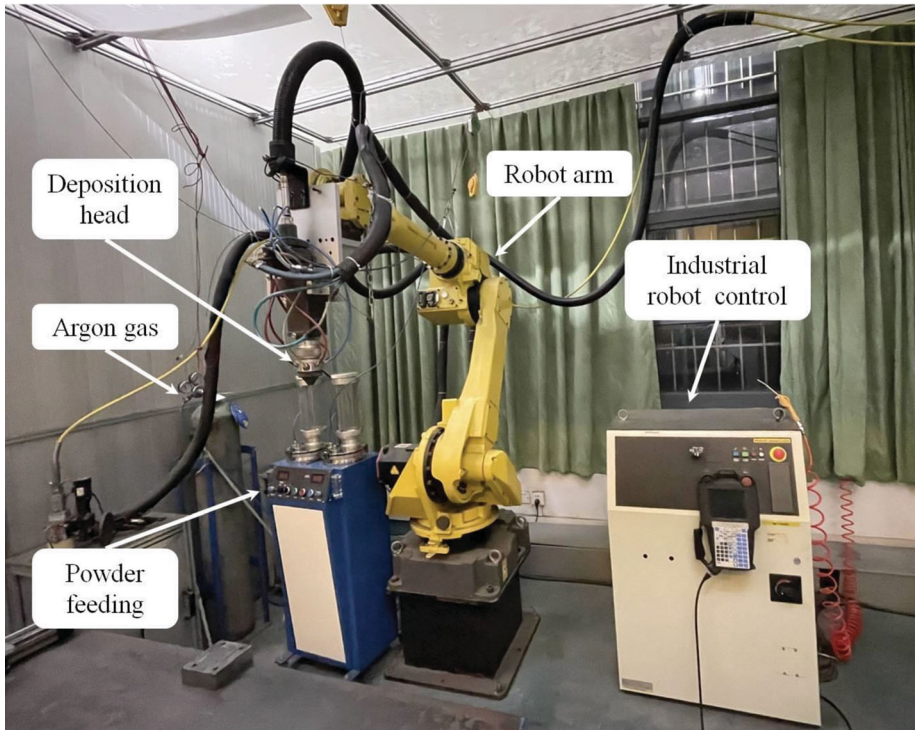

Fig. 3 Image of laser cladding system

Table 2 Matrix of variables and levels

Processing parameters	Notation	Units	Levels					
			Codes	− 2	− 1	0	1	2
Laser power	LP	W	Actual	1400	1500	1600	1700	1800
Scanning speed	SS	mm/s		4	5	6	7	8
Gas flow	GF	NL/min		16	18	20	22	24

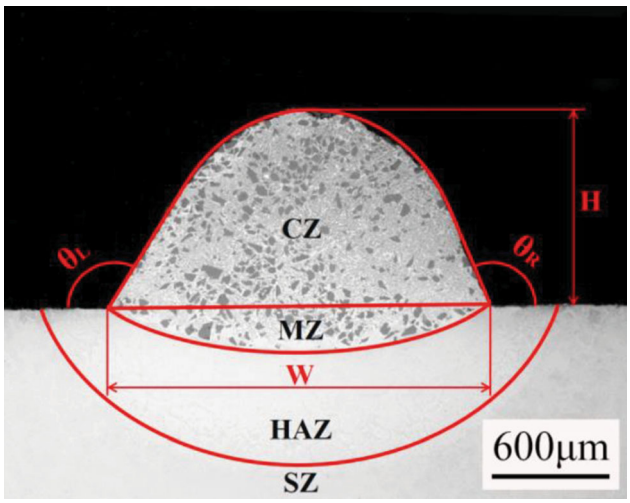

Fig. 4 Geometric structure of the cladding layer

factors. The model had a high fitting accuracy of 99.99% (Ref 23). The Adequate Precision (Signal-to-Noise Ratio) was 26.9729, greater than 4, suggesting that the model had a high degree of identification. The coefficient of the model was 0.9360, very approximating to 1. The difference between the predicted R^2 and the adjusted R^2 was less than 0.2, which indicated that the model had satisfactory prediction accuracy (Ref 24). The *P*-value of each input variable demonstrated that the cladding width was significantly affected by laser power, the interaction term between scanning speed and gas flow, and the quadratic term of laser power, followed by scanning speed and gas flow. This suggested the rationality of the input variables selection, which can effectively reveal the influence between process parameters and cladding width. The mathematical model for the cladding width is shown in Eq. (2).

Similarly, the fitting models for the clad height, cross-sectional area, and wetting angle met the accuracy requirement based on the analysis of variance. The mathematical models are provided in Eqs. (3) to (5).

$$\begin{aligned}\text{Width} = &-3.05026 + 0.011491 \times LP - 0.64706 \times SS \\ &- 0.20151 \times GF \\ &+ 0.030912 \times SS \times GF - 3.4 \times 10^{-6} \times LP^2\end{aligned} \quad \text{(Eq 2)}$$

Table 3 Experimental design and results

Run	LP, W	SS, mm/s	GF, NL/min	Width, mm	Height, mm	Area, mm^2	θ, °
1	1600	6	24	2.297	1.285	2.867	98.272
2	1500	5	22	2.174	1.436	2.072	98.145
3	1700	7	18	2.285	0.912	0.908	141.301
4	1700	7	22	2.358	1.124	2.410	107.431
5	1600	6	20	2.373	1.104	1.923	116.056
6	1600	8	20	2.267	0.828	1.198	132.307
7	1600	6	20	2.341	1.216	1.691	117.563
8	1600	6	20	2.322	1.228	2.006	125.105
9	1500	5	18	2.345	1.293	1.548	121.850
10	1600	4	20	2.432	1.752	3.097	103.908
11	1600	6	20	2.298	1.257	2.054	120.797
12	1600	6	20	2.341	1.134	2.007	124.228
13	1800	6	20	2.313	1.242	2.607	113.844
14	1600	6	16	2.437	1.178	1.220	135.218
15	1600	6	20	2.340	1.231	2.057	119.282
16	1700	5	18	2.465	1.294	2.279	123.332
17	1500	7	18	2.212	1.021	1.485	135.933
18	1500	7	22	2.269	1.095	2.343	104.759
19	1400	6	20	2.104	1.235	1.885	113.374
20	1700	5	22	2.272	1.525	3.091	93.639

Table 4 ANOVA on clad width

Source	Sum of squares	df	Mean square	*F* value	*p*-value(Prob > F)	
Model	0.132	5	0.026	40.96	< 0.0001	significant
LP	0.040	1	0.040	61.64	< 0.0001	
SS	0.013	1	0.013	20.59	0.0005	
GF	0.016	1	0.016	25.51	0.0002	
SS × GF	0.031	1	0.031	47.35	< 0.0001	
LP^2	0.032	1	0.032	49.70	< 0.0001	
Residual	9.041×10^{-3}	14	6.458×10^{-4}	…	…	
Lack of fit	5.813×10^{-3}	9	6.459×10^{-4}	1.00	0.5302	Not significant
R-squared	0.9360	…	…	Pred R-squared	0.8730	
Adj R-squared	0.9132	…	…	Adeq precision	26.9729	

Table 5 ANOVA on clad height

Source	Sum of squares	df	Mean square	*F* value	*p*-value(Prob > F)	
Model	0.711	3	0.237	65.95	< 0.0001	significant
LP	6.817×10^{-5}	1	6.817×10^{-5}	0.02	0.8922	
SS	0.662	1	0.662	184.24	< 0.0001	
GF	0.049	1	0.049	13.57	0.0020	
Residual	0.057	16	3.593×10^{-3}	…	…	
Lack of fit	0.049	11	4.424×10^{-3}	2.51	0.1604	Not significant
R-squared	0.9252	…	…	Pred R-squared	0.8702	
Adj R-Squared	0.9111	…	…	Adeq precision	30.3516	

$$\text{Height} = 1.86037 + 2.06406 \times 10^{-5} - 0.20341 \times SS + 0.027604 \times GF \quad \text{(Eq 3)}$$

$$\text{Area} = -30.05047 + 0.018646 \times LP + 4.17226 \times SS + 0.21844 \times GF - 2.828 \times 10^{-3} \times LP \times SS \quad \text{(Eq 4)}$$

Table 6 ANOVA on cross-sectional area

Source	Sum of squares	df	Mean square	*F* value	*p*-value(Prob > F)	
Model	6.130	4	1.530	30.39	< 0.0001	significant
LP	0.450	1	0.450	8.93	0.0092	
SS	1.990	1	1.990	39.41	< 0.0001	
GF	3.050	1	3.050	60.53	< 0.0001	
LP × SS	0.640	1	0.640	12.68	0.0028	
Residual	0.760	15	0.050	…	…	
Lack of Fit	0.660	10	0.066	3.44	0.0926	Not significant
R-squared	0.8902	…	…	Pred R-Squared	0.7707	
Adj R-Squared	0.8609	…	…	Adeq Precision	19.0943	

Table7 ANOVA on wetting angle

Source	Sum of squares	df	Mean square	*F* value	*p*-value(Prob > F)	
Model	3060.301	3	1020.100	58.42	< 0.0001	significant
LP	2.218	1	2.218	0.13	0.7262	
SS	746.048	1	746.048	42.73	< 0.0001	
GF	2312.035	1	2312.035	132.41	< 0.0001	
Residual	279.377	16	17.461	…	…	
Lack of Fit	234.595	11	21.327	2.38	0.1745	Not significant
R-squared	0.9163	…	…	Pred R-Squared	0.8615	
Adj R-Squared	0.9007	…	…	Adeq Precision	25.7304	

$$\theta = 190.1978 + 3.72344 \times 10^{-3} \times LP + 6.82847 \times SS - 6.01045 \times GF \quad \text{(Eq 5)}$$

Figure 5 shows the normal probability plots of residuals for the clad width, height, cross-sectional area, and wetting angle. The residual plots were following a straight line in the "S" shape, which indicated the mathematical models for each response had remarkable fitting accuracy.

Figure 6 provides a comparison between the predicted value and the actual experimental value of each response. The actual value of each response was uniformly distributed near the prediction line, indicating favorable fitting accuracy of the mathematical models due to the small errors between prediction and experiment.

3.2 Clad Width

Figure 7(a) and (b) provides the 3D-response surface and the contour line of the interaction between SS and GF on the clad width. Raising the gas flow and scanning speed simultaneously led to a decrease in the clad width. The energy input per unit time decreased with increasing the scanning speed. The powder delivery per unit time increased by enlarging the gas flow, which further weakened the energy input due to part of the powders shielding the laser. The increased scanning speed also resulted in a faster cooling rate of the molten pool, weakening the levelling trend of the pool. Thus, the clad width decreased by increasing gas flow and scanning speed.

Figure 8 presents the influence of each parameter on the clad width. Based on the figure, the clad width had a positive quadratic correlation with laser power. In addition, the clad width had a negative linear correlation with scanning speed and gas flow.

3.3 Clad Height

Table 5 indicated that the clad height was not significantly affected by neither the interaction among laser power, scanning speed, and gas flow nor laser power individually. Therefore, the influence of scanning speed and gas flow on the clad height was analyzed, respectively. In Fig. 9, the red dot indicated the clad height in the six central groups (zero level); the dotted line showed the fluctuation range of clad height under zero level. The clad height in the six central groups was concentrated within the dotted line, indicating remarkable experiment accuracy with small errors.

Figure 9(a) showed that the clad height reduced following the increase in scanning speed. Under certain laser power and gas flow, increasing scanning speed not only reduced the melted powder per unit time but also shortened energy interaction time, which led to a lower clad height. Figure 9(b) displayed that the clad height increased when raising the gas flow. The increase of gas flow resulted in more powder delivery per unit time. Under certain scanning speed and laser power, more powder melted denoted the expansion of the clad height.

3.4 Cross-Sectional Area

Figure 10 displayed the 3D response surface and the contour line of the interaction between laser power and scanning speed on the cross-sectional area. Based on Fig. 10(a) and (b), the cross-sectional area got enlarged by increasing the laser power

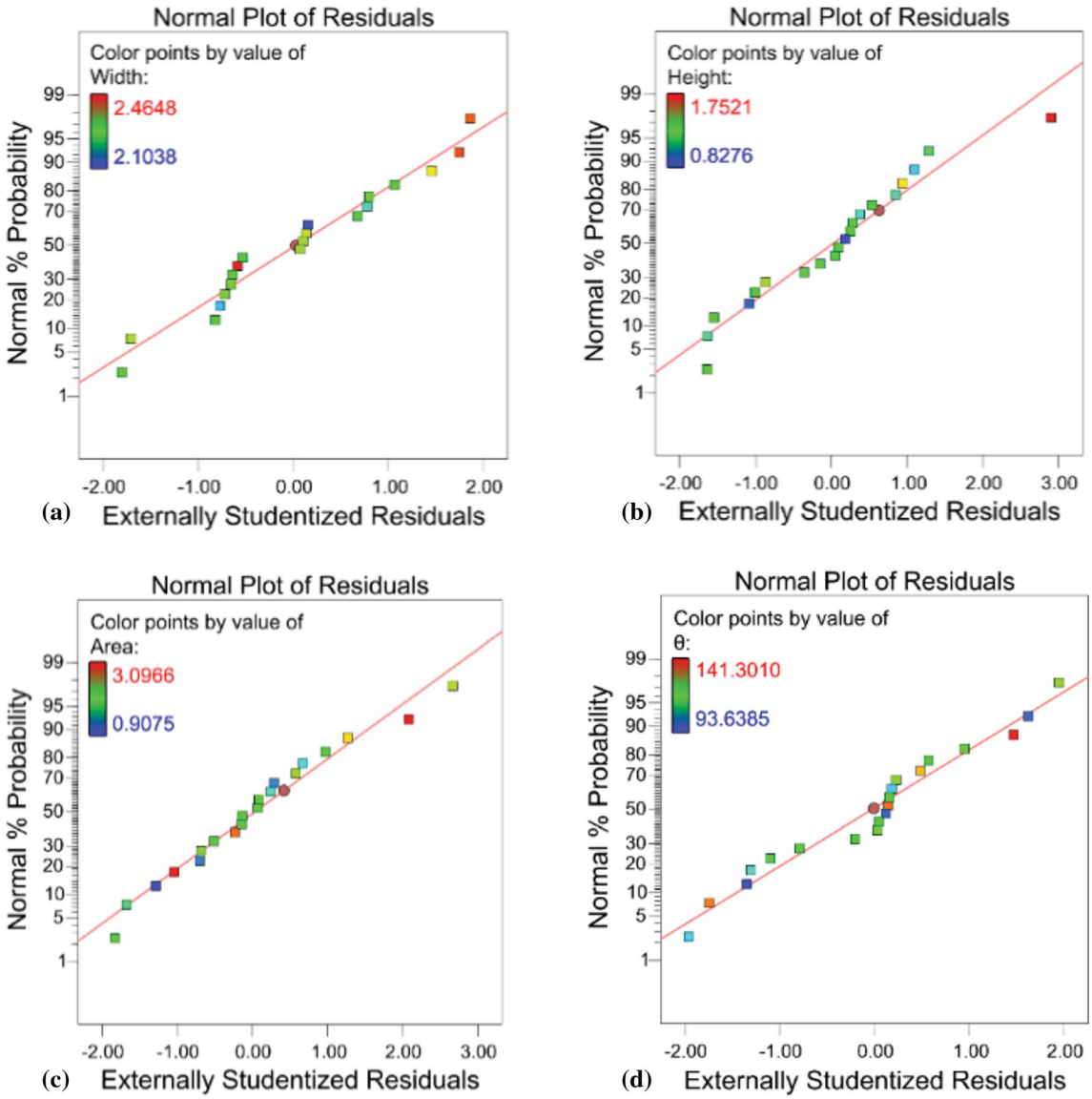

Fig. 5 Residual plots of: (a) clad width; (b) clad height; (c) cross-sectional area; (d) wetting angle

and decreasing the scanning speed. When the scanning speed was reduced, larger energy was obtained per unit time, leading to more powder in the molten pool. Meanwhile, increasing laser power added the energy input per unit time, which allowed more powder to be fully melted. The powder utilization rate was greatly improved to expand the clad area.

Figure 11 displayed the influence of each factor on the cross-sectional area. There was a linear relationship between the three factors and the cross-sectional area. The cross-sectional area was positively correlated with laser power and gas flow. On the contrary, the cross-sectional area had a negative correlation with scanning speed.

3.5 Wetting Angle

Table 7 indicated that the wetting angle was not significantly affected by neither the interaction among laser power, scanning speed, and gas flow nor laser power individually. Instead, the influence of scanning speed and gas flow on the wetting angle was extremely significant. Thus, they were analyzed in this paper. As shown in Fig. 12, the wetting angle of the six central groups (the red dots in the figure) was clustered on the dotted lines, indicating high experiment accuracy with small errors.

Figure 12(a) showed that a larger wetting angle was caused by increasing the scanning speed. When the scanning speed was raised, the laser action time was decreased per unit time,

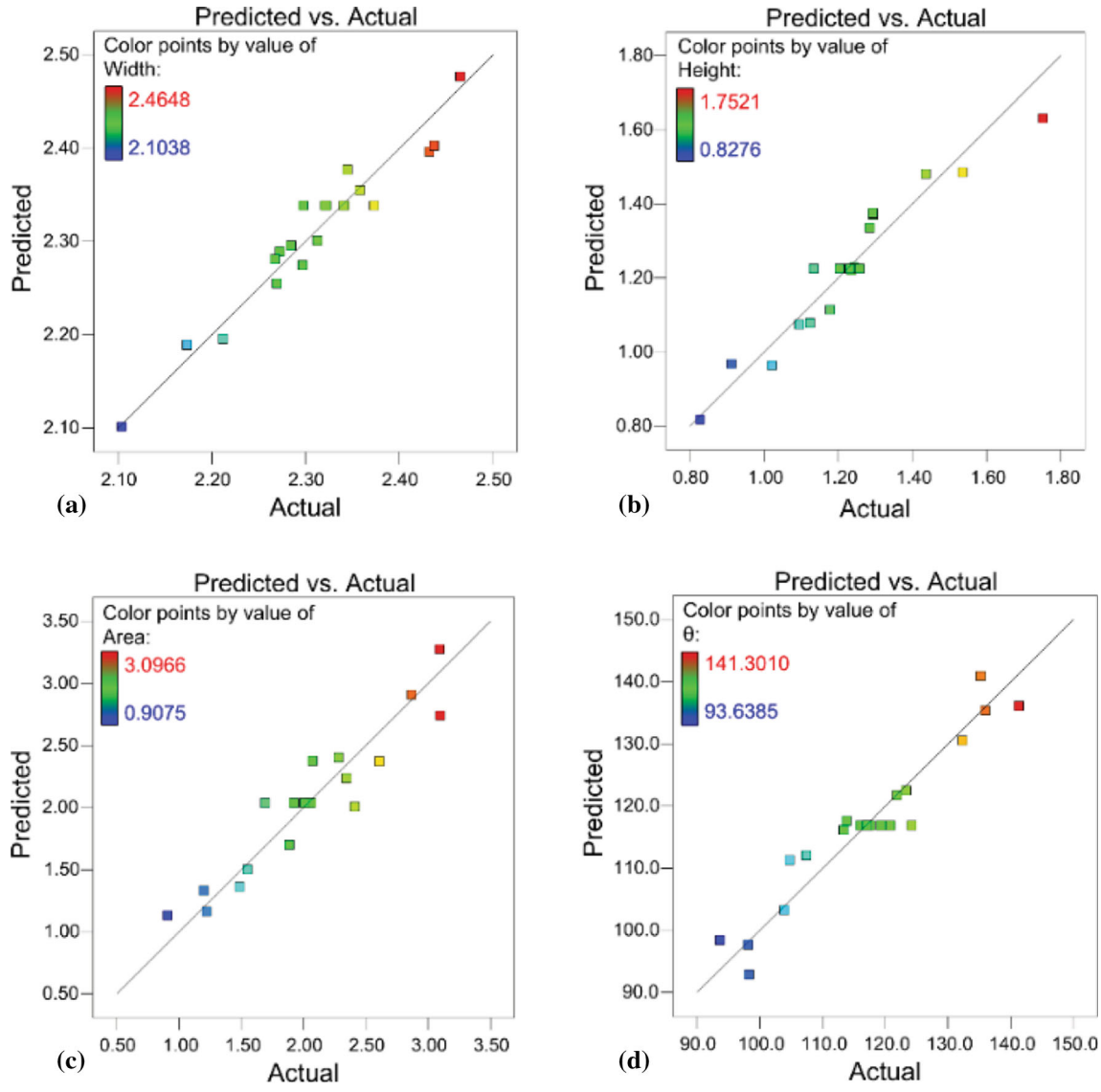

Fig. 6 Comparison of predicted and actual values for: (a) clad width; (b) clad height; (c) cross-sectional area; (d) wetting angle

which increased the cooling rate of the molten pool and shortened the action time of internal convection. This slowed down the flow of the upper part of the molten pool, hence the wetting angle was enlarged (Ref 21). Figure 12(b) displayed that the wetting angle reduced with enlarging the gas flow. Larger gas flow resulted in more molten powder per unit time. The powder accumulated on both sides, which increased the trend of powder rebounding. This leads to a smaller wetting angle.

4. Models Validation and Parameters Optimization

The process parameters require to be optimized and verified by experiments to obtain the cladding layer with outstanding geometric characteristics and to validate the accuracy of the suggested fitting models above. In the actual production process, the single-track cladding layer cannot meet the needs of large-area restoration. Multi-track overlapping is required to cover a large area. Therefore, under sufficient clad width and height, the wetting angle needs to be greater than 110° (Ref 21). This is due to the hollow overlap between the adjacent cladding tracks when the wetting angle is too small, which will lead to a higher defect rate. The height is required to be as greater as possible to ensure the height of cladding layers with single-layer multi-track overlapping because the higher height can make the surface after cladding has the secondary machining allowance. Consequently, the weights of clad width, height, cross-sectional area, and wetting angle in the optimization were considered as 3, 4, 3, and 5, respectively. Optimization was conducted with the target of the wetting angle as 120° to ensure the multi-track overlapping smoothly. Table 8 lists the optimization conditions of the parameters and goals of response values.

Table 9 provides the optimization results of the four responses, including clad width, height, cross-sectional area, and wetting angle. The table indicated that the process parameters with the highest desirability included 1700 W laser

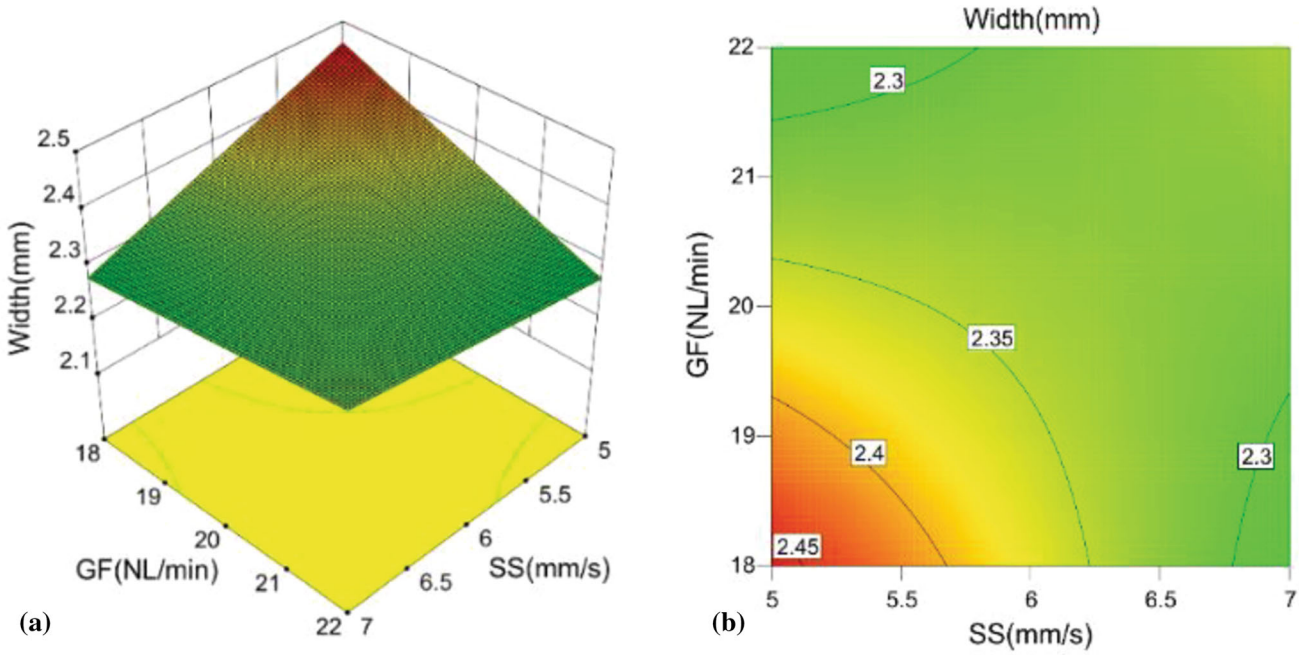

Fig. 7 (a) 3D-response surface of SS and GF affecting the clad width; (b) Contour line of SS and GF affecting the clad width

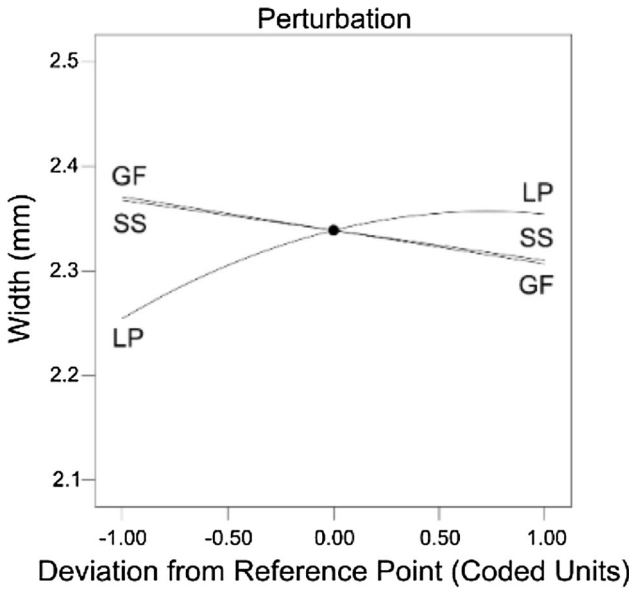

Fig. 8 Influence of each factor on the clad width

power, 5 mm/s scanning speed, and 18.413 NL/min gas flow. The selected process parameters were adjusted to 1700 W laser power, 5 mm/s scanning speed, and 18.400 NL/min gas flow considering actual experimental conditions. The experimental validation is presented in Table 9, in which the cladding layer prepared under actual experimental conditions generated the geometric characteristics, including 2.367 mm width, 1.353 mm height, 2.342 mm^2 cross-sectional area, and 120.103°wetting angle. By calculation, the error rates between experiment and prediction for clad width, height, cross-sectional area, and wetting angle were 3.702, 2.451, 6.094, and 0.085%, respectively. The small error rates indicated remarkable prediction accuracy of the mathematical models established for each response. Compared with the central groups (Fig. 13a), the optimized cladding layer (Fig. 13b) had better morphology without apparent cladding defects, better geometric characteristics in width, height, cross-sectional area, and wetting angle, and exceptional metallurgical bonding with the substrate.

The performance of the cladding layer was required to be analyzed to further determine the optimization effects. The microhardness reflects the experimental effects directly, and the microstructure provides an in-depth investigation of the influence of process parameters on the cladding layer. Therefore, the microhardness of the cladding layers in the four areas (Fig. 14a) for both the central and the optimization groups was tested. Figure 14(b) indicated a ladder-shaped distribution of the microhardness with the optimization group higher than the central group. The microhardness difference varied in a small range in the cladding zone (CZ) and became maximized in the subsurface of the cladding layer. In the process of laser cladding, the high heat conduction rate, the temperature gradient in the subsurface layer, and the high cooling rate of the molten pool hindered the growth of the grains in the layer, which led to the refinement of the structure, thus increased the microhardness.

Figure 15 provides the backscatter scanning electron microscope images and the energy spectrum of the feature areas' element composition for the subsurface of cladding layers in the central and the optimization groups. Based on the microstructure, larger laser power, lower scanning speed and gas flow increased the laser interaction time and reduced the powder delivery, which led to an increase in the energy obtained by the cladding layer to fully melt the hard particles. The larger temperature gradient was easier to be formed with higher energy, which was conducive to nucleation (Ref 25).

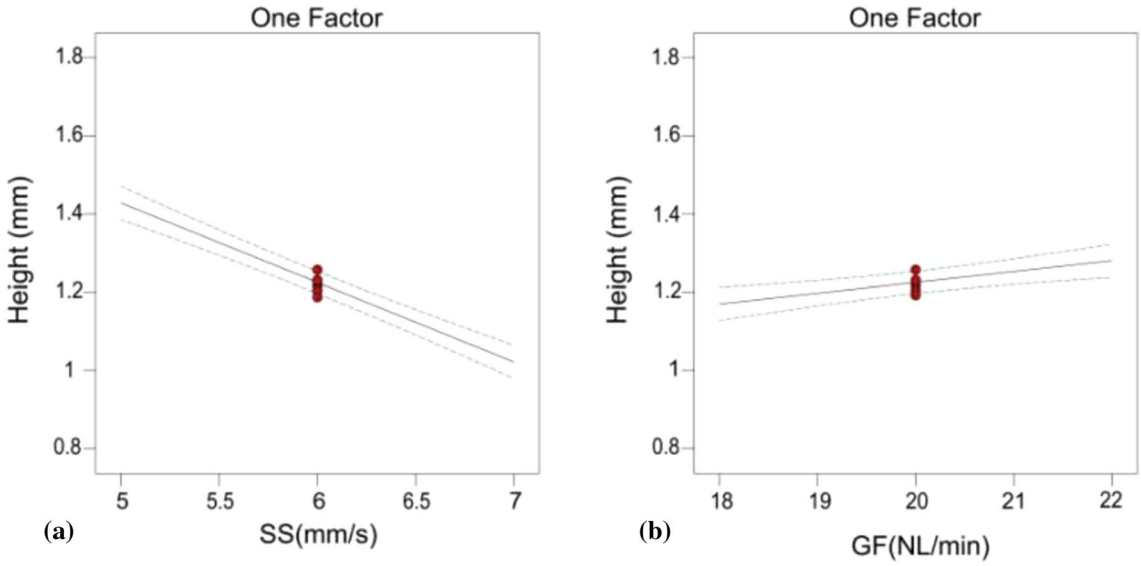

Fig. 9 (a) Influence of scanning speed on the clad height; (b) Influence of gas flow on the clad height

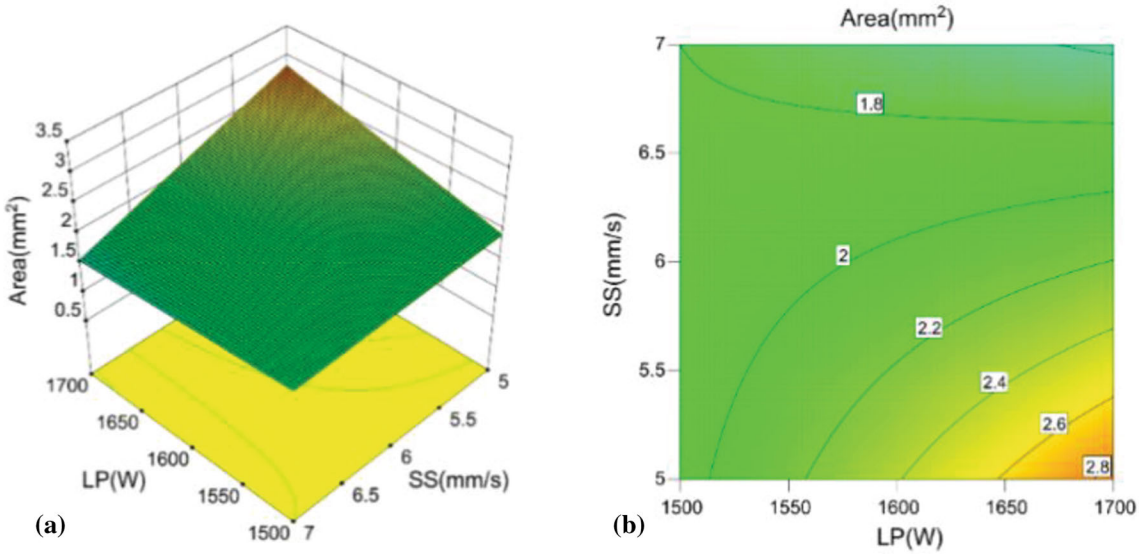

Fig. 10 (a) 3D-response surface of LP and SS affecting the cross-sectional area; (b) Contour line of LP and SS affecting the cross-sectional area

Therefore, the cladding layer in the optimization group had more refined grains with uniform distribution and higher microhardness (Ref 26). While decreasing laser power, increasing scanning speed and gas flow caused lower energy obtained by the powder. In this scenario, the cladding layer in the central group had larger initial TiC particles, and the secondary TiC particles produced by recrystallization showed an apparent transformation from equiaxed grains to dendrites. The EDS element ratio measurement for both groups displayed that the cladding layer had higher Fe and Ni contents, as shown in the bright areas (a-1 and b-1) in Fig. 15, indicating a Ni-based structure. The higher content of Ti elements in the optimization group suggested that more Ti elements were diffused into the Ni-based structure given the optimized process parameters. Meanwhile, the lower Cr content contributed to improving the microhardness of the cladding layer (Ref 26). With Ti as the main element composition, the dark areas (a-2 and b-2) were determined as TiC particles in light of the morphology and energy spectrum. In the optimization group, the initial TiC particle size was greatly reduced. The number of small-size TiC particles formed by recrystallization increased significantly. The number of dendrite crystallized particles dropped sharply. All of these indicated more decomposed Ti and higher nucleation efficiency, which strengthened dispersion. Therefore, the optimized process parameters provide necessary guidance for the forming control of single-track cladding layers on cylindrical substrates.

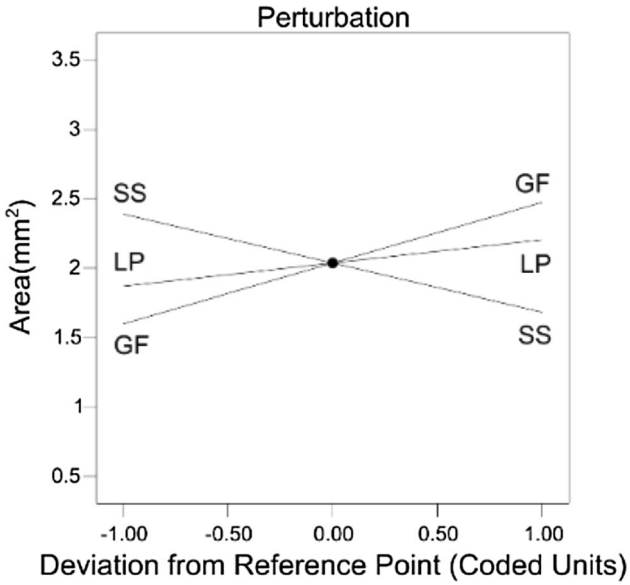

Fig. 11 Influence of each factor on the cross-sectional area

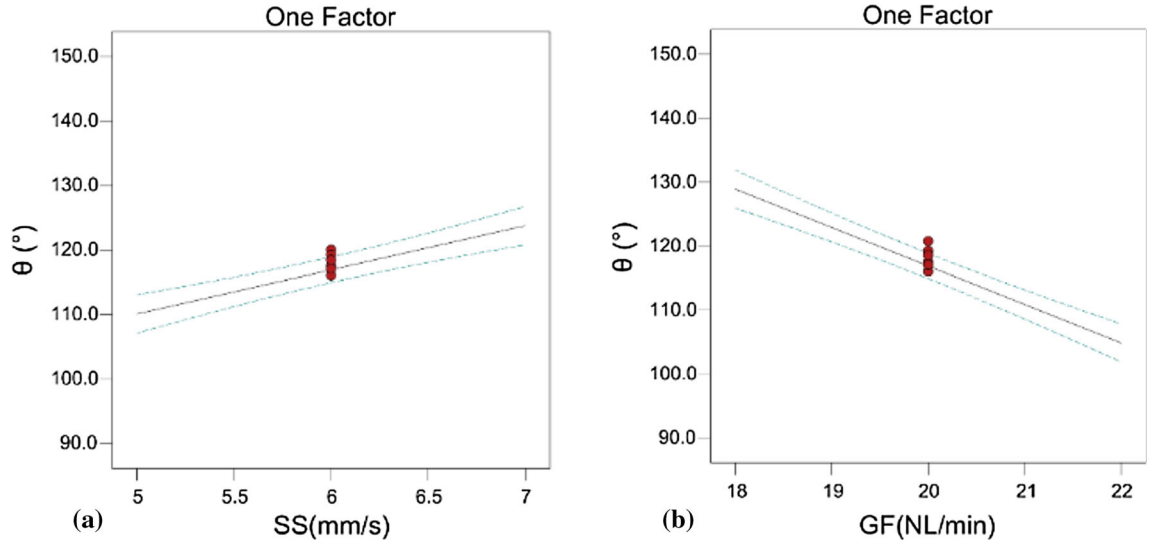

Fig. 12 (a) Influence of SS on the wetting angle; (b) Influence of GF on the wetting angle

Table 8 Conditions and goals of optimization

Name	Input/Output	Goal	Limit		Importance
			Lower	Upper	
Variables	LP,W	In range	1500	1700	3
	SS, mm/s	In range	5	7	3
	GF, NL/min	In range	18	22	3
Response	Width, mm	Maximize	2.104	2.465	3
	Height, mm	Maximize	0.828	1.752	4
	Area, mm^2	Maximize	0.908	3.097	3
	θ, °	Target = 120°	93.639	141.307	5

5. Conclusion

Based on the central composite design of response surface methodology, this paper established the mathematical models between the process parameters (laser power, scanning speed, and gas flow) and the four responses, including the width, height, cross-sectional area, and wetting angle of the single-track cladding layer on cylindrical substrates. The reliability of the model was constructed by the experimental results obtained by the optimized process parameters. The results of this study provide a reference for the forming control and prediction of single-track laser cladding on cylindrical substrate composites. The conclusions of this study were addressed as follows:

1) The clad width was most significantly affected by laser power, followed by gas flow, while scanning speed had the least significant influence on the width compared to the first two process parameters. The clad width was enlarged at first and tended to be flattened afterwards following the increase of laser power, but the rising scanning speed and gas flow reduced the clad width.

Table 9 Results of validation and optimization

	LP, W	SS, mm/s	GF, NL/min	Width, mm	Height, mm	Area, mm^2	θ, °	Desirability	
Predict	1700.000	5.000	18.413	2.458	1.387	2.494	120.000	0.817	Selected
	1699.999	5.000	18.489	2.454	1.389	2.510	119.544	0.813	
	1700.000	5.000	18.717	2.443	1.395	2.560	118.173	0.800	
	1644.869	5.000	18.379	2.459	1.385	2.238	120.000	0.799	
	1699.999	5.199	18.000	2.459	1.335	2.277	123.837	0.738	
Actual	1700.000	5.000	18.400	2.367	1.353	2.342	120.103	…	

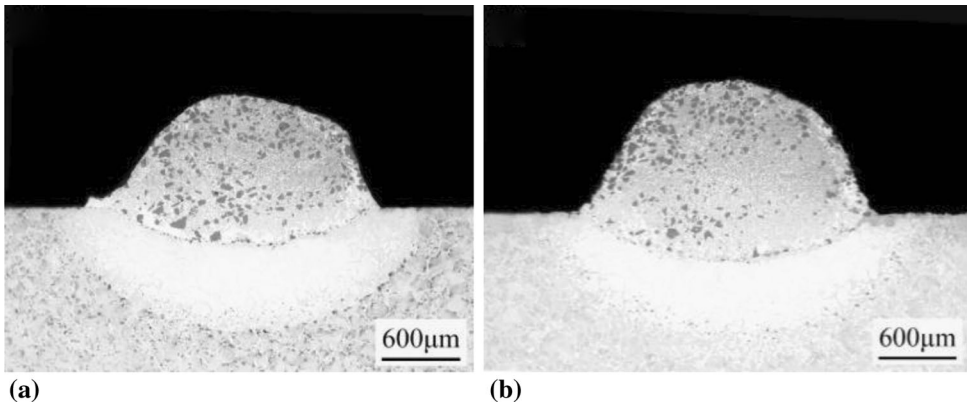

Fig. 13 (a) Micro-morphology of cladding layers in the central group (LP = 1600 W SS = 6 mm/s GF = 20 NL/min); (b) Micro-morphology of cladding layers in the optimization group (LP = 1700 W SS = 5 mm/s GF = 18.4 NL/min)

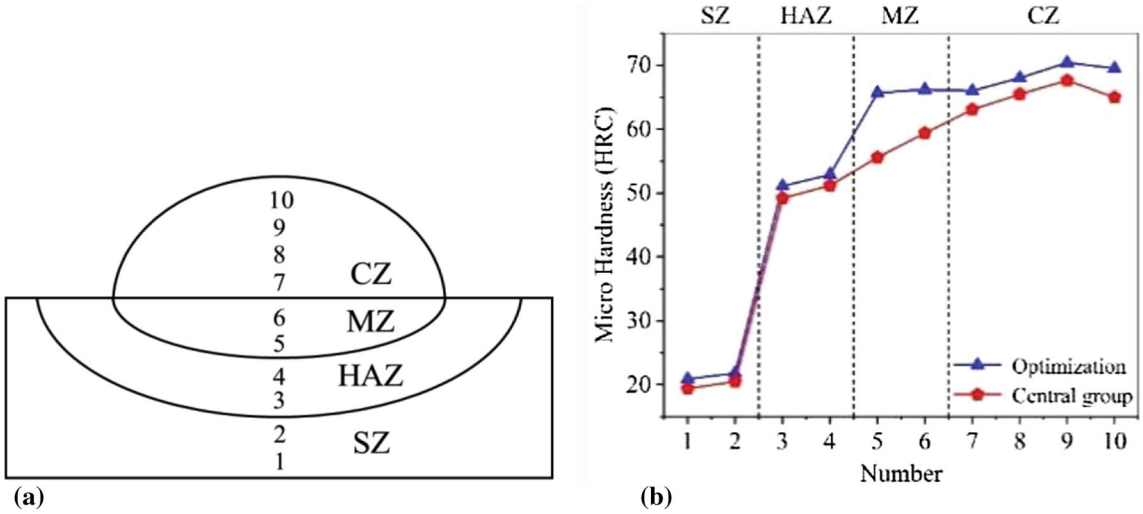

Fig. 14 (a) Schematic illustration of microhardness measurement; (b). The microhardness distribution of the cladding layer in the vertical direction

2) The significance order of influence from the process parameters on the clad height was found to be scanning speed, gas flow, and laser power. The clad height was lowered with increasing the scanning speed and enlarged by raising the gas flow.
3) The significance order of influence from the process parameters on the cross-sectional area was gas flow, scanning speed, and laser power. Simultaneously increasing the laser power and gas flow led to an increase in cross-sectional area, while the smaller cross-sectional area was caused by increasing scanning speed.
4) The wetting angle was most significantly affected by gas flow, followed by scanning speed, and it was least significantly affected by laser power. An increase and a decrease of the wetting angle were caused by raising the scanning speed and the gas flow respectively.
5) The process parameters were optimized with the goal of a 120° wetting angle and maximizing the clad width, height, and cross-sectional area. The optimized process parameters were verified by a validation experiment. The error rates between experiment and prediction for the clad width, height, cross-sectional area, and wetting angle were 3.702, 2.451, 6.094, and 0.085%, respectively.

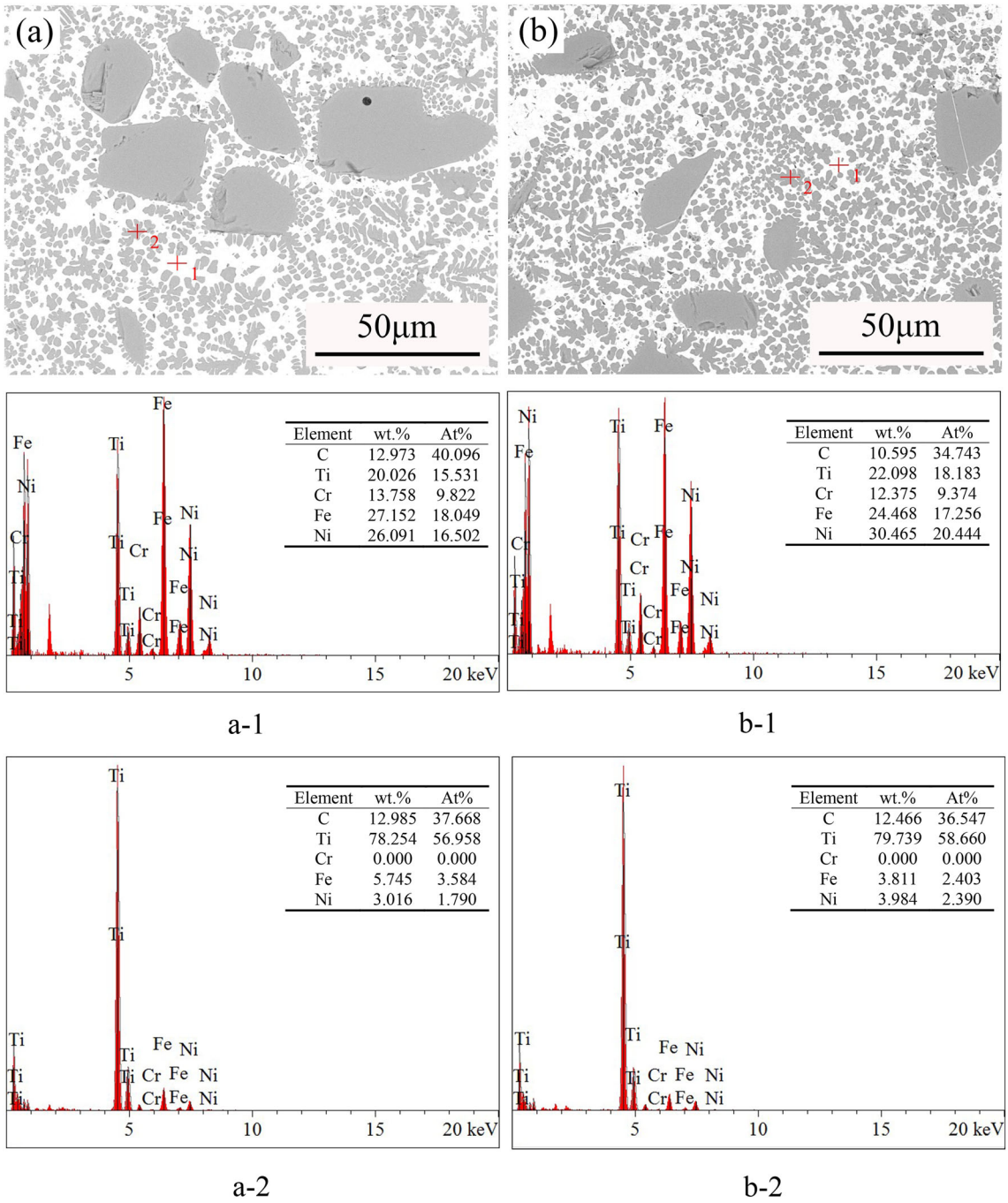

Fig. 15 (a) Microstructure and element distribution of the cladding layer in the central group; (b) Microstructure and element distribution of the cladding layer in the optimization group

Therefore, the models established in this research provide an important reference for the forming control and prediction of single-track cladding layers on cylindrical substrate composites.

Funding

This study was supported by the Science and Technology Major Project of Fujian Province (Grant No. 2020HZ03018). The authors gratefully appreciate the financial support from the Program for Innovative Research Team in Science and Technology at Fujian Province University.

Declarations

Conflict of interest

The authors declare that they have no conflict of interest.

References

1. F. Wirth and K. Wegener, A Physical Modeling and Predictive Simulation of the Laser Cladding Process, *Addit. Manuf.*, 2018, **22**, p 307–319. (**in English**)
2. M. Alizadeh-Sh, S.P.H. Marashi, E. Ranjbarnodeh et al., Dissimilar Laser Cladding of Inconel 718 Powder on A-286 Substrate: Microstructural Evolution, *J. Las. Appl.*, 2020, **32**(2), p 022048. (**in English**)
3. M. Alizadeh-Sh, S.P.H. Marashi, E. Ranjbarnodeh et al., Prediction of Solidification Cracking by an Empirical-Statistical Analysis for Laser Cladding of Inconel 718 Powder on a Non-Weldable Substrate, *Optic. Las. Technol.*, 2020, **128**, p 106244. (**in English**)
4. B. Song, T. Yu, X. Jiang et al., Development Mechanism and Solidification Morphology of Molten Pool Generated by Laser Cladding, *Inter. J. Therm. Sci.*, 2021, **159**, p 106579. (**in English**)
5. A.A. Siddiqui and A.K. Dubey, Recent Trends in Laser Cladding and Surface Alloying, *Optic. Las. Technol.*, 2021, **134**(8), p 106619. (**in English**)
6. F. Wirth, S. Arpagaus and K. Wegener, Analysis of Melt Pool Dynamics in Laser Cladding and Direct Metal Deposition by Automated high-Speed Camera Image Evaluation, *Addit. Manuf.*, 2018, **21**, p 369–382. (**in English**)
7. N. Ur Rahman, L. Capuano, A. Van Der Meer et al., Development and Characterization of Multilayer Laser Cladded High Speed Steels, *Addit. Manuf.*, 2018, **24**, p 76–85. (**in English**)
8. O.B. Kovalev, D.V. Bedenko and A.V. Zaitsev, Development and Application of Laser Cladding Modeling Technique: From Coaxial Powder feeding to Surface Deposition and Bead Formation, *Appl. Math. Model.*, 2018, **57**, p 339–359. (**in English**)
9. B. Bax, R. Rajput, R. Kellet et al., Systematic Evaluation of Process Parameter Maps for Laser Cladding and Directed Energy Deposition, *Addit. Manuf.*, 2018, **21**, p 487–494. (**in English**)
10. P. Shayanfar, H. Daneshmanesh and K. Janghorban, Parameters Optimization for Laser Cladding of Inconel 625 on ASTM A592 Steel, *J. Market. Res.*, 2020, **9**(4), p 8258–8265. (**in English**)
11. Y. Javid, Multi-Response Optimization in Laser Cladding Process of WC Powder on Inconel 718, *CIRP J. Manuf. Sci. Technol.*, 2020, **31**, p 406–417. (**in English**)
12. P. Fan and G. Zhang, Study on Process Optimization of WC-Co50 Cermet Composite Coating by Laser Cladding, *Inter. J. Refract. Metals Hard Mater.*, 2020, **87**, p 105133. (**in English**)
13. A. Khorram, A. Davoodi Jamaloei, M. Paidar et al., Laser Cladding of INCONEL 718 with 75Cr3C2 + 25(80Ni20Cr) Powder: Statistical Modeling and Optimization, *Surf. Coat. Technol.*, 2019, **378**, p 124933. (**in English**)
14. F. Bourahima, A.L. Helbert, M. Rege et al., Laser Cladding of Ni Based Powder on a Cu-Ni-Al Glassmold: Influence of the Process Parameters on Bonding Quality and Coating Geometry, *J. Alloy. Compd.*, 2019, **771**, p 1018–1028. (**in English**)
15. C. Barr, S. Da Sun, M. Easton et al., Influence of Macrosegregation on Solidification Cracking in Laser Clad Ultra-High Strength Steels, *Surf. Coat. Technol.*, 2018, **340**, p 126–136. (**in English**)
16. A. Calleja, I. Tabernero, A. Fernández et al., Improvement of Strategies and Parameters for Multi-Axis Laser Cladding Operations, *Opt. Lasers Eng.*, 2014, **56**, p 113–120. (**in English**)
17. N. Jeyaprakash, M. Duraiselvam and S.V. Aditya, Numerical Modeling of WC-12% Co Laser Alloyed Cast Iron in High Temperature Sliding Wear Condition Using Response Surface METHODOLOGY, *Surf. Rev. Lett.*, 2018, **25**(07), p 1950009. (**in English**)
18. K.I. Yaakob, M. Ishak, M.M. Quazi et al., Optimizing the Pulse Wave Mode low Power Fibre Laser Welding Parameters of 22Mnb5 Boron Steel Using Response Surface Methodology, *Measurement*, 2019, **135**, p 452–466. (**in English**)
19. Y. Liu, J. Zhang, Z. Pang et al., Investigation into the Influence of Laser Energy Input on Selective Laser Melted Thin-Walled Parts by Response Surface Method, *Opt. Lasers Eng.*, 2018, **103**, p 34–45. (**in English**)
20. R.S. Vidyarthy, D.K. Dwivedi and V. Muthukumaran, Optimization of A-TIG Process Parameters Using Response Surface Methodology, *Mater. Manuf. Process.*, 2017, **33**(7), p 709–717. (**in English**)
21. T. Yu, L. Yang, Y. Zhao et al., Experimental Research and Multi-Response Multi-Parameter Optimization of Laser Cladding Fe313, *Opt. Laser Technol.*, 2018, **108**, p 321–332. (**in English**)
22. A. Balaram Naik and R.A. Chennakeshava, Optimization of Tensile Strength in TIG Welding Using the Taguchi Method and Analysis of Variance (ANOVA), *Thermal Sci. Eng. Progress*, 2018, **8**, p 327–339. (**in English**)
23. M. Erfanmanesh, H. Abdollah-Pour, H. Mohammadian-Semnani et al., An Empirical-Statistical Model for Laser Cladding of WC-12Co Powder on AISI 321 Stainless Steel, *Opt. Laser Technol.*, 2017, **97**, p 180–186. (**in English**)
24. E.O. Olakanmi, S.T. Nyadongo, K. Malikongwa et al., Multi-Variable optimisation of the Quality Characteristics of Fiber-Laser Cladded Inconel-625 Composite Coatings, *Surf. Coat. Technol.*, 2019, **357**, p 289–303. (**in English**)
25. J.P. Oliveira, A.D. Lalonde and J. Ma, Processing Parameters in Laser Powder bed Fusion Metal Additive Manufacturing, *Mater. Des.*, 2020, **193**, 108762. (**in English**)
26. T. Han, M. Xiao, Y. Zhang et al., Effect of Cr Content on Microstructure and Properties of Ni-Ti-xCr Coatings by Laser Cladding, *Optik*, 2019, **179**, p 1042–1048. (**in English**)